Microstructural control of porous In_2O_3 powders prepared by ultrasonic-spray pyrolysis employing self-synthesized polymethylmethacrylate microspheres as a template and their NO_2-sensing properties

Takeo Hyodo*, Eriko Fujii, Keijiro Ishida, Taro Ueda, and Yasuhiro Shimizu

Graduate School of Engineering, Nagasaki University

1-14 Bunkyo-machi, Nagasaki 852-8521, Japan

*Corresponding author:

Takeo Hyodo, Dr.

Graduate School of Science and Technology, Nagasaki University

1-14 Bunkyo-machi, Nagasaki 852–8521, Japan

Tel: +81–95–819–2644

Fax: +81–95–819–2643

E-mail: hyodo@nagasaki-u.ac.jp

Abstract

NO_2-sensing properties of porous In_2O_3 powders prepared by ultrasonic-spray pyrolysis employing self-synthesized polymethylmethacrylate (PMMA) microspheres as a template have been investigated in this study. The PMMA microspheres were synthesized by ultrasonic-assisted emulsion polymerization. The pore-size distribution, crystallite size (CS), and specific surface area (SSA) of the porous In_2O_3 powders prepared with the PMMA microspheres with a diameter of ca. 77 nm (pr-In_2O_3(T_p), T_p: pyrolysis temperature, *600–1100* (ºC)) are largely dependent on the pyrolysis temperature of the ultrasonic-spray pyrolysis. On the other hand, the porous In_2O_3 powder prepared by ultrasonic-spray pyrolysis at 1100ºC employing PMMA microspheres with a diameter of ca. 26 nm (pr-In_2O_3(T_p)S) had larger pore volume and smaller SSA than the pr-In_2O_3(*1100*) powder, whereas the CS of the pr-In_2O_3(T_p)S powder was comparable to that of the pr-In_2O_3(*1100*) powder. The pr-In_2O_3(T_p) and pr-In_2O_3(*1100*)S sensors (T_p: *600* or *1100*) showed larger response and faster response speed to 10 ppm NO_2 than the conventional In_2O_3 sensor (the sensor fabricated with In_2O_3 powder prepared by ultrasonic-spray pyrolysis without PMMA microspheres at 1100ºC) at lower temperatures, because of their well-developed porous structure, small CS, and large SSA. In addition, the magnitude of response of the pr-In_2O_3(*1100*) sensor to 10 ppm NO_2 was larger than that of the pr-In_2O_3(6*00*) sensor at less than 250ºC, whereas smaller CS and larger SSA of the pr-In_2O_3(6*00*) powder were effective in improving the magnitude of response to NO_2 at a low concentration. The pr-In_2O_3(*1100*)S sensor showed relatively larger response and faster response speed to NO_2 at a low concentration than the pr-In_2O_3(*1100*) sensor at lower temperatures, which probably indicated that the well-developed medium pores was important for enhancing these NO_2-sensing properties.

***Keywords*:** NO_2 sensor; porous In_2O_3 powder; ultrasonic-spray pyrolysis;

polymethylmethacrylate microsphere; ultrasonic-assisted emulsion polymerization

1. Introduction

Since gas-sensing properties of semiconducting oxides as chemiresistors were reported in 1962 [1, 2], various kinds of semiconductors have been demonstrated as gas-sensing materials or transducers for different types of gas sensors, such as diodes [3–7], field-effect transistors (FETs) [8–11], varistors [12–16], and thermoelecric devices [17–20], as well as the chemiresistors [21–25]. Nowadays, some semiconducting oxides have been useful also as gas-sensing electrode materials for electrochemical gas sensors [26–30]. Optimal design of their microstructure is indispensable for enhancing their gas-sensing properties, because the gas diffusivity in these materials is one of important factors in determining the magnitude of gas response, and the response and recovery speeds, together with the gas reactivity on the surface of these materials. Therefore, various nanostructured materials such as nanoparticles [31, 32], nanowires [33, 34], nanotubes [35, 36], hollow microspheres [37–40], and various porous materials [41–43] have been suggested as promising gas-sening materials. Our efforts have also been directed to developing well-developed mesoporous and/or macroporous gas-sensing materials (centered pore size: ca. 2–50 nm for mesopores, ≥ 150 nm for macropores) by utilizing some templates in the past 20 years or so, to enhance the gas sensitivity and selectivity of various types of gas sensors [44–65]. Mesoporous gas-sensing materials were prepared by utilizing a self-assembly of various surfactants such as *n*-cetylpyridinium chloride ($CH_3(CH_2)_{15}C_5H_5NCl$, $C_{16}PyCl$) and a triblock copolymer (e.g., Pluronic P123 (BASF Corp., $HO(CH_2CH_2O)_{20}(CH_2CH(CH_3)O)_{70}(CH_2CH_2O)_{20}H$), MW: ca. 5800) as a template, and they showed quite large responses to various gases, because of the well-developed mesopores (small pores with a diameter of several nanometers (centered pore size: < ca. 6.0 nm, which was quite dependent on the template used), small crystallite size (CS, e.g. 1.5–4.0 nm for mesoporous SnO_2), and large specific surface area (SSA, e.g. 250–380 $m^2\ g^{-1}$ for mesoporous SnO_2) [44–51]. However, the gas sensors fabricated with these mesoporous materials generally had some

disadvantages such as relatively large resistance and slow recovery speed. On the other hand, macroporous gas-sensing materials were prepared by a modified sol-gel technique [52–57], ultrasonic-spray pyrolysis [58–61], or physical vapor deposition technique [62, 63] employing polymethylmethacrylate (PMMA) microspheres (Soken Chem. & Eng. Co., Ltd., typical particle size: 150, 400, 800, and 1500 nm in diameter) as a template, and the introduction of spherical macropores (e.g., 600–700 nm in diameter, for PMMA microspheres with a diameter of 800 nm) into the materials was effective in improving the gas response as well as the fast response and recovery speeds. However, the magnitude of gas responses of the macroporous materials was generally smaller than those of the mesoporous ones, because the macroporous materials had relatively larger CS and smaller SSA than the mesoporous ones. Therefore, we have recently attempted to synthesize PMMA microspheres with well-controlled particle size of less than 150 nm by ultrasonic-assisted emulsion polymerization, to prepare porous gas-sensing materials having medium pores (targeted diameter: several nm – less than 100 nm), smaller CS, and larger SSA, by ultrasonic-spray pyrolysis employing the synthesized PMMA microspheres [64, 65].

In this study, the effects of synthesis condition of the PMMA microspheres by ultrasonic-assisted emulsion polymerization on the size of the PMMA microspheres have been investigated. In addition, the NO_2-sensing properties of porous In_2O_3 prepared by ultrasonic-spray pyrolysis employing the synthesized PMMA microspheres have been estimated in dry air, to clarify the effects of the porous structures, CS, and SSA on the magnitude of NO_2 response and the response and recovery speeds.

2. Experimental

2.1 Synthesis of PMMA microspheres

PMMA microspheres were synthesized by ultrasonic-assisted emulsion polymerization.

Methyl methacrylate monomer (MMA; Wako Pure Chem. Ind., Ltd., 150 cm^3) was washed for three times with 0.05 M NaOH aqueous solution (1 dm^3), to remove a polymerization inhibitor from the MMA monomer. The pure MMA monomer obtained (8 g), sodium lauryl sulfate (SLS; Nacalai Tesque, Inc., 0.1 g) as a surfactant and ammonium persulfate (Wako Pure Chem. Ind., 0.3 g) as an initiator were added to deionized water (100 cm^3), and then the resultant oil/water (o/w) emulsion was ultrasonically treated by an ultrasonic homogenizer (Nissei Corp., US-150T, 19.5 ± 1 kHz). The polymerization of MMA to PMMA was initiated in the micelles, just upon the irradiation of strong ultrasonic wave to the o/w emulsion at room temperature (RT), and the temperature of the o/w emulsion increased from RT to ca. 65°C within 15 min. After the ultrasonic irradiation for 5–150 min, the aqueous dispersion containing PMMA microspheres was obtained. The conversion ratio from MMA to PMMA was caluculated by measiring the weight of PMMA residues remained after vacuum drying of the aqueous dispersions (1 cm^3) which were collected during the ultrasonic treatment. The particle-size distribution of the synthesized PMMA microspheres in the aqueous dispersion was measured at 25°C by dynamic light scattering (DLS; Malvern Instrument Ltd., HPPS).

2.2 Preparation of pr-In_2O_3 powders by ultrasonic spray pyrolysis

The aqueous dispersion containing PMMA microspheres (37.5 cm^3) was mixed with 0.05 mol dm^{-3} $In(NO_3)_3$ aqueous solution (62.5 cm^3) and the mixture was served as an aqueous precursor solution. Figure S1 shows schematic drawing of a feeding system of the aqueous precursor solution atomized by ultrasonication (namely, mists) into an electric furnace. A specially designed mist-supplier for the ultrasonic-spray pyrolysis was used to get uniform mists of the precursor solution. Various sizes of mists of the precursor solution were generated in a plastic container equipped with a polyethylene thin film at one end, which was perpendicularly set over an ultrasonic vibrator (Honda Electric Co., Ltd., HM-303N, 2.4 MHz)

at a distance of 0.5–1.0 cm in water. The mists were carried into a glass vessel by air flowing No. 1 (1.5 dm^3 min^{-1}), and only small droplets were allowed to move into an electric furnace heated at 600–1100ºC with an assistance of air flowing No. 2 (1.5 dm^3 min^{-1}). As the mists were momentarily heated at the electric furnace, the evaporation of water and the thermal decomposition of $In(NO_3)_3$ and PMMA microspheres simultaneously happened and spherical indium oxide powders are produced in the air flow in the electric furnace. The obtained porous powders were denoted as pr-In_2O_3(T_p) (T_p: pyrolysis temperature in the electric furnace, 600–1100ºC). A conventional In_2O_3 (c-In_2O_3(T_p), T_p: 600 or 1100(ºC)) powder was also prepared by the similar preparation technique employing a PMMA-free $In(NO_3)_3$ aqueous solution, for a comparative purpose. The pr-In_2O_3(T_p) and c-In_2O_3(T_p) powders were heat-treated at 550ºC for 5 h in ambient air, which is the same heat-treatment temperature as the sensor fabrication, because we need to know the microstructure of the sensors fabricated with the powders as accurately as possible.

The microstructure of the obtained In_2O_3 powders was observed by scanning electron microscopy (SEM; JEOL Ltd., JSM-7500F) and transmission electron microscopy (TEM; JEOL Ltd., JEM2010). The pore-size distribution and specific surface area (SSA) of the In_2O_3 powders were measured by Barrett–Joyner–Halenda (BJH) and Brunauer–Emmett–Teller (BET) methods using N_2 adsorption-desorption isotherms (Micromeritics Instrument Corp., Tristar3000), respectively. Crystal phase of the In_2O_3 powders was characterized by X-ray diffraction analysis (XRD; Rigaku Corp., RINT2200) using Cu Kα radiation (40 kV, 40 mA), and their crystallite size (CS) was calculated from the (222) diffraction peak using Scherrer equation.

2.3 Fabrication of thick film sensors and measurement of their gas sensing properties

Thick film sensors were fabricated by screen printing employing the paste of each In_2O_3

powder on an alumina substrates equipped with a pair of interdigitated Pt electrodes (gap size: ca. 200 μm), followed by calcination at 550°C for 5 h in ambient air. Gas responses of these sensors were measured to 1.0, 5.0, and 10 ppm NO_2 balanced with dry air at a flow rate of 100 cm^3 min^{-1} at 150–500°C. The magnitude of response to NO_2 was defined as the ratio (R_g/R_a) of sensor resistance in NO_2 balanced with air (R_g) to that in air (R_a).

3. Results and Discussions

3.1 Characterizations of PMMA microspheres and representative pr-In_2O_3(T_p) and c-In_2O_3(T_p) powders

Figure 1 shows variation in conversion ratio from MMA to PMMA with sonication time and representative particle-size distributions of PMMA microspheres synthesized in an o/w emulsion. Many MMA monomers of more than 80% were quickly polymerized and the particle size gradually increased in the first 15 min with a rise in the temperature from RT to ca. 65ºC, due to the polymerization in the micelles, and the size of all the PMMA microspheres was distributed in comparatively narrow range. In addition, the conversion ratio from MMA to PMMA and the size of PMMA microspheres remained almost unchanged after 30 min. Therefore, the ultrasonic polymerization was stopped at 30 min later after the start of the polymerization, and the obtained aqueous dispersion containing PMMA microspheres (average particle size: ca. 77 nm) was used as a base liquid for ultrasonic spray pyrolysis.

Figure S2 shows XRD spectra of pr-In_2O_3(*600*) and pr-In_2O_3(*1100*) powders as-prepared and after heat treatment at 550ºC for 5 h, together with their crystallite size (CS). All peaks of these XRD patterns were assigned to cubic In_2O_3 (JCPDF: 6-416). The CS of the as-prepared pr-In_2O_3(*1100*) powder (ca. 18.3 nm) was much larger than that of the as-prepared pr-In_2O_3(*600*) powder (ca. 2.6 nm), because the pyrolysis treatment at higher temperatures promoted the sintering among the crystallites. The heat treatment at 550°C for 5 h drastically increased the

CS of the pr-In_2O_3(*600*) powder. On the other hand, the heat treatment hardly changed the CS of the pr-In_2O_3(*1100*) powder, because the pyrolysis temperature of the pr-In_2O_3(*1100*) powder (1100°C) is much higher than the heat-treatment temperature (550°C). Figures S3 and 2 shows N_2 adsorption-desorption isotherms and pore-size distributions of pr-In_2O_3(*600*) and pr-In_2O_3(*1100*) powders as-prepared and after heat treatment at 550ºC for 5 h, together with their specific surface area (SSA). In addition, Figs. 3 and 4 show their SEM and TEM photographs, respectively. The as-prepared pr-In_2O_3(*600*) powder had well-developed medium pores with centered diameters of ca. 60–70 nm and ca. 30 nm, which were calculated from N_2 adsorption and desorption isotherms, respectively, because the as-prepared pr-In_2O_3(*600*) powder had an hysteresis loop in the N_2 adsorption-desorption curves in the relatively high pressure range (see Fig. S3). The centered diameter of ca. 60–70 nm was roughly correspondent to the size of internal spherical pores in the pr-In_2O_3(*600*) particles (ca. 50–65 nm), which were observed in the TEM photographs (Fig. 4(a)). The spherical pores seemed to originate from the morphology of the PMMA microspheres, but the pore size was slightly smaller than the average diameter of the PMMA microspheres (ca. 77 nm). These results show that the PMMA microspheres synthesized by the ultrasonic-assisted emulsion polymerization were effectively utilized as a template to introduce the well-developed porous structure into spherical In_2O_3 particles. On the other hand, the centered diameter of ca. 30 nm which were calculated from the N_2 desorption isotherm was almost correspondent to the size of circular pores on the surface of the pr-In_2O_3(*600*) particles, which were observed in the SEM and TEM photographs (Figs. 3(a) and 4(a)), probably because only a part of the PMMA microspheres and a connection between PMMA microspheres was served as a template for the surficial pores. These results indicate that the well-developed spherical pores of the as-prepared pr-In_2O_3(*600*) powder consist of narrow necks (ca. 30 nm) and wide bodies (60–70 nm) as ink-bottle porous morphology. In addition, the as-prepared pr-In_2O_3(*600*) powder also had a large amount of small pores with a

diameter of less than 5 nm, and thus the SSA (ca. 53.8 m^2 g^{-1}) was really large. However, the geometric surface area (GSA) of the as-prepared pr-In_2O_3(*600*) powder, which was calculated from the density and the CS (ca. 2.6 nm, see Fig. S2) obtained from their XRD spectra, is ca. 321 m^2 g^{-1}, assuming that the morphology of their crystallites with the density of 7.180 g cm^{-3} [66] is spherical. Namely, the GSA was much larger than the SSA (53.8 m^2 g^{-1}). This indicated that most of the small In_2O_3 crystallites were densely connected with each other, which restricted the large amount of N_2 adsorption on the crystallite surface. As the In_2O_3 crystallites, which form the relatively smooth oxide frameworks for the spherical porous structure of the as-prepared pr-In_2O_3(*600*) powder, are actually quite small, the boundaries among the crystallites are also not clear, in the TEM photographs (Fig. 4(a)). On the other hand, the SSA of the pr-In_2O_3(*600*) powder after the heat treatment (ca. 55.8 m^2 g^{-1}) was comparable to that of the as-prepared pr-In_2O_3(*600*) powder (ca. 53.8 m^2 g^{-1}), even though the CS of the pr-In_2O_3(*600*) powder after the heat treatment (ca. 10.6 nm) was much larger than that of the as-prepared pr-In_2O_3(*600*) powder (ca. 2.6 nm). In addition, the crystallite growth distorted the shape of oxide frameworks and partly seemed to collapse the frameworks, as shown in the TEM photographs (Fig. 4(a)ii)). As the GSA of the pr-In_2O_3(*600*) powder after the heat treatment was ca. 78.8 m^2 g^{-1}, the large crystallites of the pr-In_2O_3(*600*) powder after the heat treatment seem to have relatively large surface with some grain boundaries, in comparison with small crystallites of the as-prepared pr-In_2O_3(*600*) powder. Such morphology was confirmed also in the TEM photographs (Fig. 4(a)ii)). These microstructural change in the pr-In_2O_3(*600*) powder is probably the reason why the large SSA of the pr-In_2O_3(*600*) powder was maintained in spite of the large CS, even after the heat treatment at 550ºC. In addition, the heat treatment extremely decreased the volume of the medium pores with a centered diameter of around 30 nm and 60–70 nm, and increased the pore volume from ca. 1 nm to ca. 20 nm in diameter overall. These results also indicate that spherical pores in the particles was partly collapsed after the heat

treatment, but the surface morphology of the particles remained almost unchanged, as shown in the SEM photographs (Fig. 3(a)).

The as-prepared pr-In_2O_3(*1100*) powder showed much smaller SSA (ca. 19.9 m^2 g^{-1}) than that of the as-prepared pr-In_2O_3(*600*) powder, together with the large CS. The SSA was much smaller than the GSA (ca. 45.7 m^2 g^{-1}), probably because of relatively many connections among the large crystallites (i.e., crystallite boundaries), as shown in the TEM photographs (Fig. 4(b)), but the surface morphology of the as-prepared pr-In_2O_3(*1100*) powder, which was observed by SEM, was really comparable to that of the as-prepared pr-In_2O_3(*600*) powder (see Fig. 3). The pore-size distribution of the as-prepared pr-In_2O_3(*1100*) powder was similar to that of the as-prepared pr-In_2O_3(*600*) powder. Namely, the as-prepared pr-In_2O_3(*1100*) powder also had well-developed medium pores with centered diameters of ca. 50–70 nm and ca. 33 nm, which were calculated from N_2 adsorption and desorption isotherms, respectively, and the result indicates that the medium pores also consist of narrow necks and wide bodies (ink-battle pores). However, the pore volume of the as-prepared pr-In_2O_3(*1100*) powder was smaller than that of the as-prepared pr-In_2O_3(*600*) powder in all the pore-diameter range, and the size of the oxide frameworks of the pr-In_2O_3(*1100*) powder was larger than that of the pr-In_2O_3(*600*) powder, which was dependent on the CS (see Fig. 4). The heat treatment at 550°C for 5 h seems to have little effect on the SSA, pore-size distribution, and the microstructure of the pr-In_2O_3(*1100*) powder (see Figs. 2–4), as is the case with the CS (see Fig. S2), because the pyrolysis temperature was much higher than the heat-treatment temperature. Only the morphology of the In_2O_3 crystallites slightly changed after the heat treatment.

Figure 5 summarized variations in CS and SSA of all the pr-In_2O_3(T_p) powders as-prepared and after heat treatment at 550ºC for 5 h with pyrolysis temperature (T_p), together with those of representative c-In_2O_3(T_p) powders as-prepared and after heat treatment at 550ºC for 5 h. The CS of both the pr-In_2O_3(T_p) and c-In_2O_3(T_p) powders increased and their SSA decreased with

an increase in pyrolysis temperature (T_p), because of the crystallite growth at elevated temperatures. In addition, the heat treatment tended to increase the SSA of the pr-In_2O_3(T_p) powders, even though the CS increased with the heat treatment. This is because the heat treatment at a lower temperature (550ºC) for a longer period (5 h) than ultrasonic-spray pyrolysis (T_p: 600–1100ºC, air-flow velocity in the electric furnace: 1.53 m min^{-1}, average retention time at T_p: ca. 4 s) had some morphological effects on agglomerates of the In_2O_3 crystallites, such as sintering among the crystallites, reduction in the crystallite boundaries, increase in smaller pores (< 20 nm in diameter), and so on. In addition, the CS of the pr-In_2O_3(T_p) powders was smaller than that of the c-In_2O_3(T_p) powders, while the SSA of the pr-In_2O_3(T_p) powders was much larger than that of the c-In_2O_3(T_p) powders. Figure 6 shows SEM and TEM photographs of the as-prepared c-In_2O_3(*1100*) powder, as a representative of c-In_2O_3(T_p) powders. The c-In_2O_3(*1100*) particles were roughly spherical with about 200–500 nm in diameter, and the TEM photograph showed that the bulk was really dense. In addition, the GSA calculated with the CS of the c-In_2O_3(*1100*) powder (ca. 24.7 nm) was ca. 33.8 m^2 g^{-1}, which supports that the c-In_2O_3(*1100*) particles were almost dense with less pores, and each In_2O_3 particle consisted of many crystallites.

3.2 NO_2-sensing properties of pr-In_2O_3(*600*), pr-In_2O_3(*1100*), and c-In_2O_3(*1100*) sensors

Figure S4 shows cross-sectional SEM photographs of pr-In_2O_3(*600*), pr-In_2O_3(*1100*), and c-In_2O_3(*1100*) sensors. These sensors were fabricated with single or triple stacking of an In_2O_3 film by screen printing, because thickness of the sensing In_2O_3 films is one of important factors in determining the NO_2-sensing properties. Consequently, the film thickness of the triple-layered c-In_2O_3(*1100*) sensor was almost comparable to those of single-layered pr-In_2O_3(*600*) and pr-In_2O_3(*1100*) sensors. Figure 7 shows response transients of pr-In_2O_3(*600*), pr-In_2O_3(*1100*), and c-In_2O_3(*1100*) sensors to 10 ppm NO_2 at 200ºC in dry air, as representatives.

The resistance of the c-In_2O_3(*1100*) sensor in dry air was the largest among them. In addition, an increase in pyrolysis temperature resulted in a decrease in the resistance of the pr-In_2O_3(*T*p) sensors. The thickness of all the sensors had an insignificant effect on the resistance in dry air, but an increase in the thickness tended to decrease and increase the magnitude of NO_2 responses of the pr-In_2O_3(*T*p) sensors and the c-In_2O_3(*1100*) sensor at 200ºC, respectively. Furthermore, the pr-In_2O_3(*T*p) sensors apparently showed larger NO_2 response and faster response and recovery speeds than those of the c-In_2O_3(*1100*) sensor at 200ºC.

Figure 8 shows variations in response of all the sensors to 10 ppm NO_2 and 90% response time with operating temperature. The 90% response time contains a delay period from the gas-switching time to the response-starting time, ca. 64 s, in this study, since the dead volume of the gas-flow pathway and the chamber in the measurement apparatus is ca. 106 cm^3. The magnitude of NO_2 responses of the pr-In_2O_3(*T*p) sensors was larger than that of the c-In_2O_3(*1100*) sensors at lower temperatures (≤ 300ºC), and it monotonically tended to decrease with a rise in the operating temperature over the whole operating temperature range. In addition, the magnitude of NO_2 responses of the pr-In_2O_3(*1100*) sensors was larger than that of the pr-In_2O_3(*600*) sensors, only in the operating temperature range of less than 250ºC, even though the pr-In_2O_3(*1100*) powder had larger CS and smaller SSA than those of the pr-In_2O_3(*600*) powder (see Fig. 5). Considering that small CS and larger SSA was generally effective in improving the gas-sensing properties [21, 22, 31–33, 45–49], the well-developed medium pores of the pr-In_2O_3(*1100*) powder may be the most important factor in enhancing the magnitude of NO_2 responses at the lower temperatures. The magnitude of NO_2 responses of the c-In_2O_3(*1100*) sensor was comparable to that of the pr-In_2O_3(*T*p) sensors at higher temperatures (≥ 350ºC). As the magnitude of NO_2 response of the c-In_2O_3(*1100*) sensors decreased with a decrease in the operating temperature at lower temperatures (≤300ºC), the magnitude of NO_2 responses of the pr-In_2O_3(*T*p) sensors was much larger than that of the c-In_2O_3(*1100*) sensors in the lower

temperature range. These results certainly arise from the larger CS and smaller SSA of pr-In_2O_3(*T*p) powders than those of c-In_2O_3(*1100*) powder (see Fig. 5). On the other hand, the 90% response time of the pr-In_2O_3(*T*p) sensors was shorter than that of the c-In_2O_3(*1100*) sensors, especially at lower temperatures (≤ 350ºC). These results apparently indicate that various sizes of pores which were well-developed in the spherical In_2O_3 powders largely improved the response speeds at the lower temperatures and thus the NO_2 diffusivity in the pr-In_2O_3(*T*p) powders must be much better than that in the c-In_2O_3(*1100*) powder. However, the CS and SSA also complicatedly seem to have an impact on the response speeds as well as the magnitude of NO_2 responses of these sensors. An increase in thickness of the pr-In_2O_3(*T*p) films slightly decreased the magnitude of their NO_2 responses and that of the c-In_2O_3(*1100*) film largely increased the magnitude of the NO_2 response only at lower temperatures (≤ 200ºC for the pr-In_2O_3(*T*p) sensors and ≤ 300ºC for the c-In_2O_3(*1100*) sensor), while the difference in thickness of these films hardly showed systematic change in their 90% response times, probably because there were unexpected voids and cracks in their films.

Figure 9 shows variations in response of all the sensors to 1 and 5 ppm NO_2 in dry air with the operating temperature. The c-In_2O_3(*1100*) sensors showed little response to 1 ppm NO_2 (R_g/R_a: < 2), while the pr-In_2O_3(*T*p) sensors maintained sufficiently large responses even to 1 ppm NO_2 (e.g., R_g/R_a: ca. 200 at 200ºC for pr-In_2O_3(*600*) sensor (film thickness: ca. 69 μm). This result indicates that the introduction of well-developed porous structure into the powders was quite effective in improving the response especially to NO_2 at a low concentration, in dry air. In addition, the pr-In_2O_3(*600*) sensors tended to show relatively larger responses to NO_2 at a low concentration than the pr-In_2O_3(*1100*) sensors, over the whole temperature range. This result shows that the small CS and large SSA effectively improved the magnitude of responses to NO_2 at a low concentration.

3.3 Synthesis of smaller PMMA microspheres and effects of introduction of smaller medium pores into pr-In_2O_3 particles on the NO_2-sensing properties

As mentioned above, the size control of the porous structure in spherical In_2O_3 particles prepared by ultrasonic-spray pyrolysis is one of effective techniques in enhancing their NO_2-sensing properties. Therefore, reduction in the size of PMMA microspheres has been attempted by an increase in the amount of the sodium lauryl sulfates (SLS) in the aqueous precursor solution which was used for synthesis of PMMA microspheres, to reduce the size of medium pores in the In_2O_3 particles. Figure 10 shows variations in average particle size of PMMA microspheres in o/w emulsions, which was measured by DLS, and conversion ratio from MMA to PMMA for 30 min with the amount of SLS added to deionized water (100 cm^3) for synthesis of PMMA microspheres. The MMA monomers in the aqueous precursor solution was polymerized at a considerable conversion ratio (over 80%), and the conversion ratio slightly tended to increase with an increase in the amount of SLS added in the aqueous precursor solution. On the other hand, the average particle size of PMMA microspheres drastically decreased with an increase in the amount of SLS added, probably because an increase in the amount of SLS in the o/w emulsion reduced the size of micelles. The particle-size distribution of the PMMA microspheres which were synthesized in the o/w emulsion containing 0.5 g SLS was shown in Fig. 10(i), as a representative. The average particles size of the PMMA microspheres was ca. 26 nm, and the distribution was really narrow. In this study, the PMMA microspheres were utilized as a template for the preparation of pr-In_2O_3 powder by ultrasonic-spray pyrolysis at 1100ºC, and the obtained pr-In_2O_3 powder was denoted as pr-In_2O_3(*1100*)S.

Figure 11 shows pore-size distributions of pr-In_2O_3(*1100*)S powders as-prepared and after heat treatment at 550ºC for 5 h, together with their SSA and CS. The as-prepared pr-In_2O_3(*1100*)S powder also had well-developed medium pores, and the centered diameters, ca. 25–30 nm and ca. 15–20 nm, which were calculated from N_2 adsorption and desorption

isotherms, respectively, were smaller than those of as-prepared pr-In_2O_3(*T*p) powders (ca. 60–70 nm and ca. 30 nm, respectively, see Fig. 2). The smaller size of medium pores reflects the morphology of the small PMMA microspheres with an average diameter of ca. 26 nm. The heat treatment at 550ºC for 5 h has a slight effect on the pore-size distribution and the CS, and the pore volume of these medium pores maintained even after the heat treatment. However, the heat treatment decreased the SSA from 18.6 m^2 g^{-1} to 12.3 m^2 g^{-1}, probably because the heat treatment reduced the amount of small pores which were formed among In_2O_3 crystallites. Figure 12 shows SEM and TEM photographs of the as-prepared pr-In_2O_3(*1100*)S powder. Quite numerous well-developed smaller medium pores (around 20 nm in diameter) were confirmed to be on the surface of the particles, in comparison with medium pores on the surface of the pr-In_2O_3(*1100*) particles (see Fig. 3). The size of well-developed medium pores in the pr-In_2O_3(*1100*)S particles, which was too small and/or broad to confirm the porous morphology clearly in the TEM photographs, seems to be smaller than that of the pr-In_2O_3(*1100*) particles.

Figure 13 shows response transients of the pr-In_2O_3(*1100*)S sensor to 10 ppm NO_2 at 200ºC in dry air, together with those of the pr-In_2O_3(*1100*) and c-In_2O_3(*1100*) sensors, which had the similar thickness of the In_2O_3 film as the pr-In_2O_3(*1100*)S sensor (thickness of the In_2O_3 film: ca. 20 μm). In addition, Fig. 14 shows variations in response of pr-In_2O_3(*600*), pr-In_2O_3(*1100*), and c-In_2O_3(*1100*) sensors to 10 ppm NO_2 and their 90% response time with operating temperature. The pr-In_2O_3(*1100*)S sensor showed large NO_2 response at lower temperatures. The response of the pr-In_2O_3(*1100*)S sensor to 10 ppm NO_2 also monotonically increased with a decrease in the operating temperature, but the magnitude of the NO_2 response was smaller than that of the pr-In_2O_3(*1100*) sensor over the whole temperature range. Therefore, the magnitude of response of the pr-In_2O_3(*1100*)S sensor to 10 ppm NO_2 was only larger than that of the c-In_2O_3(*1100*) sensor at lower temperatures (≤ 250ºC). Furethermore, the pr-In_2O_3(*1100*)S sensor showed relatively fast response and recovery speeds as shown in Fig. 13,

and the 90% response time of the pr-In_2O_3(*1100*)S sensor was almost shorter than that of the pr-In_2O_3(*1100*) sensor as well as the c-In_2O_3(*1100*) sensor (see Fig. 14). Especially, the response behavior of the pr-In_2O_3(*1100*)S sensor right after the inlet of 10 ppm NO_2 in dry air, which is not directly reflected in the 90% response time in Fig. 14, was quite fast at lower temperatures. Figure 15 shows variations in response of pr-In_2O_3(*1100*)S, pr-In_2O_3(*1100*), and c-In_2O_3(*1100*) sensors to 1 and 5 ppm NO_2 in dry air with operating temperature, together with response transients of the pr-In_2O_3(*1100*)S sensor to 1 and 5 ppm NO_2 at 150 and 250ºC. The response and recovery speeds of the pr-In_2O_3(*1100*)S sensor to 1 and 5 ppm NO_2 tended to become slow with a decrease in the operating temperature, but the pr-In_2O_3(*1100*)S sensor showed clear NO_2 response behavior with the large responses, even in the lower temperature range. In addition, the magnitude of NO_2 response of the pr-In_2O_3(*1100*)S sensor was larger than that of the pr-In_2O_3(*1100*) sensor, with a decrease in the operating temperature. These results showed that the introduction of smaller medium pores into the In_2O_3 particles was more effective in improving the magnitude of NO_2 response, especially at a lower NO_2 concentration and lower temperatures.

Conclusion

The pr-In_2O_3(T_p) and pr-In_2O_3(*1100*)S powders (T_p: *600–1100* (ºC)) were prepared by ultrasonic-spray pyrolysis employing self-synthesized PMMA microspheres with a diameter of ca. 77 nm and ca. 26 nm, respectively, and the NO_2-sensing properties of the pr-In_2O_3(T_p) and pr-In_2O_3(*1100*)S sensors (T_p: *600* or *1100*) were investigated in dry air, together with those of the c-In_2O_3(*1100*) sensor. The pr-In_2O_3(T_p) powders had smaller CS and larger SSA than the c-In_2O_3(*1100*) powder, and the CS increased and the SSA decreased with an increase in the pyrolysis temperature. The well-developed medium pores of the pr-In_2O_3(*600*) powder decreased after heat treatment, while those of the pr-In_2O_3(*1100*) powder was less dependent on the heat treatment. The pr-In_2O_3(T_p) sensors (T_p: *600* or *1100*) showed larger response and faster

response speed to 10 ppm NO_2 than those of the c-In_2O_3(*1100*) sensor at lower temperatures (≤ 300ºC), which probably result from well-developed porous structure, smaller CS, and larger SSA of the pr-In_2O_3(T_p) powders. In addition, the magnitude of response of the pr-In_2O_3(*1100*) sensor to 10 ppm NO_2 was larger than that of the pr-In_2O_3(6*00*) sensor in the operating temperature range of less than 250ºC, but smaller CS and larger SSA of the pr-In_2O_3(T_p) powder seems to be effective in improving the magnitude of response to NO_2 at a low concentration. On the other hand, the pr-In_2O_3(*1100*)S powder had larger medium-pore volume than the pr-In_2O_3(*1100*) powder, and thus the pr-In_2O_3(*1100*)S sensor showed relatively fast response to NO_2 and larger responses to NO_2 at a low concentration than the pr-In_2O_3(*1100*) sensor, at lower temperatures.

References

1. T. Seiyama, A. Kato, K. Fujishi, M. Nagatani, A new detector for gaseous components using semiconductive thin films, Anal. Chem. 34 (1962) 1502–1503.
2. N. Taguchi, Published patent application in Japan, S37-47677, October (1962).
3. S. Tonomura, T. Matsuoka, N. Yamamoto, H. Tsubomura, Metal-semiconductor junctions for the detection of reducing gases and the mechanism of the electrical response, Nippon Kagaku Kaishi 10 (1980) 1585–1590.
4. B. P. Luther, S. D. Wolter, S. E. Mohney, High temperature Pt Schottky diode gas sensors on n-type GaN, Sens. Actuators B 56 (1999) 164–168.
5. Y Shimizu, N Kuwano, T Hyodo, M. Egashira, High H_2 sensing performance of anodically oxidized TiO_2 film contacted with Pd, Sens. Actuators B 83 (2002) 195–201.
6. T. Hyodo, M. Nakaoka, Y. Shimizu, M. Egashira, Diode-type H_2 sensors using anodized TiO_2 films —structural and compositional controls of noble metal sensing electrodes, Sens. Lett. 9 (2011) 641-645.
7. T. Hyodo, T. Yamashita, Y. Shimizu, Effects of surface modification of noble-metal sensing electrodes with Au on the hydrogen-sensing properties of diode-type gas sensors employing an anodized titania film, Sens. Actuators B 207 (2015) 105–116.
8. I. Lundström, S. Shivaraman, C. Svensson, L. Lundkvist, A hydrogen-sensitive MOS field-effect transistor, Appl. Phys. Lett. 26 (1975) 55–56.
9. Y. Gurbuz, W. P. Kang, J. L. Davidson, D. L. Kinser, D. V. Kerns, Diamond microelectronic gas sensors, Sens. Actuators B 33 (1996) 100–104.
10. I. Eisele, T. Doll, M. Burgmair, Low power gas detection with FET sensors, Sens. Actuators B 78 (2001) 19–25.
11. C. Bura, M. Bastuck, A. L. Spetz, M. Andersson, A. Schütz, Selectivity enhancement of SiC-FET gas sensors by combining temperature and gate bias cycled operation using

multivariate statistics, Sens. Actuators B 193 (2014) 931–940.

12. F.-C. Lin, Y. Takao, Y. Shimizu, M. Egashira, Preparation and H_2 sensing properties of ZnO varistor gas sensors, Denki Kagaku (presently Electrochemistry) 61 (1993) 1021–1022.
13. F.-C. Lin, Y. Takao, Y. Shimizu, and M. Egashira, ‘‘Zinc oxide varistor gas sensors: I, effect of Bi_2O_3 content on the H_2-sensing properties, J. Am. Ceram. Soc. 78 (1995) 2301–2306.
14. Y. Shimizu, F.-C. Lin, Y. Takao, M. Egashira, Zinc oxide varistor gas sensors: II, effect of chromium(III) oxide and yttrium oxide additives on the hydrogen-sensing properties, J. Am. Ceram. Soc. 81 (1998) 1633–1643.
15. T. Hyodo, Y. Baba, K. Wada, Y. Shimizu, M. Egashira, Hydrogen sensing properties of SnO_2 varistors loaded with SiO_2 by surface chemical modification with diethoxydimethylsilane, Sens. Actuators B 64 (2000) 175–181.
16. Y. Shimizu, N. Nakashima, T. Hyodo, M. Egashira, NOx sensing properties of varistor-type gas sensors consisting of micro p-n junctions, J. Electroceram. 6 (2001) 209–217.
17. M. Matsumiya, F. Qiu, W. Shin, N. Izu, N. Murayama, S. Kanzaki, Thin-film Li-doped NiO for thermoelectric hydrogen gas sensor, Thin Solid Films 419 (2002) 213-217.
18. W. Shin, M. Matsumiya, N. Izu, N. Murayama, Hydrogen-selective thermoelectric gas sensor, Sens. Actuators B 93 (2003) 304–308.
19. F. Rettig, R. Moos, Direct thermoelectric gas sensors: Design aspects and first gas sensors, Sens. Actuators B 123 (2007) 413–419.
20. F. Rettig, R. Moos, Direct thermoelectric hydrocarbon gas sensors based on SnO_2, IEEE Sensors Journal 7 (2007) 1490–1496.
21. N. Yamazoe, New approaches for improving semiconductor gas sensors, Sens. Actuators B 5 (1991) 7–19.
22. A. Gurlo, M. Ivanovskaya, N. Bârsan, M. Schweizer-Berberich, U. Weimar, W. Göpel, A.

Diéguez, Grain size control in nanocrystalline In_2O_3 semiconductor gas sensors, Sens. Actuators B 44 (1997) 327–333.

23. M. C. Carotta, M. Ferroni, D. Gnani, V. Guidi, M. Merli, G. Martinelli, M. C. Casale, M. Notaro, Nanostructured pure and Nb-doped TiO_2 as thick film gas sensors for environmental monitoring, Sens. Actuators B 58 (1999) 310–317.
24. N. Izu, W. Shin, N. Murayama, Fast response of resistive-type oxygen gas sensors based on nano-sized ceria powder, Sens. Actuators B 93 (2003) 449–453.
25. N. Yamazoe, K. Shimanoe, Theory of power laws for semiconductor gas sensors, Sens. Actuators B 128 (2008) 566–573.
26. G. Y. Lu, N. Miura, N. Yamazoe, High-temperature hydrogen sensor based on stabilized zirconia and a metal oxide electrode, Sens. Actuators B 35 (1996) 130–135.
27. M. Ono, K. Shimanoe, N. Miura, N. Yamazoe, Amperometric sensor based on NASICON and NO oxidation catalysts for detection of total NOx in atmospheric environment, Sens. Actuators B 136–137 (2000) 583–588.
28. M. Mori, H. Nishimura, Y. Itagaki, Y. Sadaoka, Potentiometric VOC detection in air using 8YSZ-based oxygen sensor modified with $SmFeO_3$ catalytic layer, Sens. Actuators B 142 (2009) 141–146.
29. T. Goto, T. Hyodo, T. Ueda, K. Kamada, K. Kaneyasu, Y. Shimizu, CO-sensing properties of potentiometric gas sensors using an anion-conducting polymer electrolyte and Au-loaded metal oxide electrodes, Electrochim. Acta 166 (2015) 232–243.
30. T. Hyodo, T. Goto, T. Ueda, K. Kaneyasu, Y. Shimizu, Potentiometric carbon monoxide sensors using an anion-conducting polymer electrolyte and Au-loaded SnO_2 electrodes, J. Electrochem. Soc. 163 (2016) B300-B308.
31. N.-S. Baik, G. Sakai, N. Miura, N. Yamazoe, Hydrothermally treated sol solution of tin oxide for thin-film gas sensor, Sens. Actuators B 63 (2000) 74–79.

32. M. Epifani, E. Comini, R. Díaz, J. Arbiol, P. Siciliano, G. Sberveglieri, J. R. Morante, Oxide nanopowders from the low-temperature processing of metal oxide sols and their application as gas-sensing materials, Sens. Actuators B 118 (2006) 105–109.

33. C. Baratto, E. Comini, G. Faglia, G. Sberveglieri, M. Zha, A. Zappettini, Metal oxide nanocrystals for gas sensing, Sens. Actuators B 109 (2005) 2–6.

34. P. Andrei, L. L. Fields, J. P. Zheng, Y. Cheng, P. Xiong, Modeling and simulation of single nanobelt SnO_2 gas sensors with FET structure, Sens. Actuators B 128 (2007) 226–234.

35. O. K. Varghese, D. Gong, M. Paulose, K. G. Ong, C. A. Grimes, Hydrogen sensing using titania nanotubes, Sens. Actuators B 93 (2003) 338–344.

36. M.-H. Seo, M. Yuasa, T. Kida, J.-S. Huh, N. Yamazoe, K. Shimanoe, Detection of organic gases using TiO_2 nanotube-based gas sensors, Proc. Chem. 1 (2009) 192-195.

37. L. You, X. He, D. Wang, P. Sun, Y. F. Sun, X. S. Liang, Y. Du, G. Y. Lu, Ultrasensitive and low operating temperature NO_2 gas sensor using nanosheets assembled hierarchical WO3 hollow microspheres, Sens. Actuators B 173 (2012) 426–432.

38. J.-W. Yoon, Y. J. Hong, G. D. Park, S.-J. Hwang, F. Abdel-Hady, A. A. Wazzan, Y. C. Kang, J.-H. Lee, Kilogram-scale synthesis of Pd-loaded quintuple-shelled Co_3O_4 microreactors and their application to ultrasensitive and ultraselective detection of methylbenzenes, Appl. Mater. Interfaces, 7 (2015) 7717-7723.

39. Y. J. Hong, J.-W. Yoon, J.-H. Lee, Y. Ch. Kang, One-pot synthesis of Pd-loaded SnO_2 yolk-shell nanostructures for ultraselective methyl benzene sensors, Chem. Eur. J. 20 (2014) 2737-2741.

40. J.-H. Lee**,** Gas sensors using hierarchical and hollow oxide nanostructures: overview, Sens. Actuators B, 140 (2009) 319-336.

41. G. Li, S. Kawi, MCM-41 modified SnO_2 gas sensors: sensitivity and selectivity properties, Sens. Actuators B 59 (1999) 1–8.

42. M. Tiemann, Porous metal oxides as gas sensors, Chem. Eur. J., 13 (2007) 8376–8388.

43. T. Wagner, T. Sauerwald, C.-D. Kohl, T. Waitz, C. Weidmann, M. Tiemann, Gas sensor based on ordered mesoporous In_2O_3, Thin Solid Films, 517 (2009) 6170–6175.

44. T. Hyodo, N. Nishida, Y. Shimizu, M. Egashira, Preparation and gas-sensing properties of thermally stable mesoporous SnO_2, Sens. Actuators B, 83 (2002) 209–215.

45. T. Hyodo, S. Abe, Y. Shimizu, M. Egashira, Gas-sensing properties of ordered mesoporous SnO_2 and effects of coatings thereof, Sens. Actuators B 93 (2003) 590–600.

46. M. Hayashi, T. Hyodo, Y. Shimizu, M. Egashira, Effects of microstructure of mesoporous SnO_2 powders on their H_2 sensing properties, Sens. Actuators B 141 (2009) 465–470.

47. Y. Shimizu, A. Jono, T. Hyodo, M. Egashira, Preparation of large mesoporous SnO_2 powder for gas sensor application, Sens. Actuators B 108 (2005) 56–61.

48. G. S. Devi, T. Hyodo, Y. Shimizu, M. Egashira, Synthesis of mesoporous TiO_2-based powders and their gas-sensing properties, Sens. Actuators B 87 (2002) 122–129.

49. C. Yu, T. Hyodo, Y. Shimizu, M. Egashira, Preparation of thermally stable mesoporous TiO_2 powder and its gas sensor application, Electrochemistry 71 (2003) 475–480.

50. T. Hyodo, Y. Mitsuyasu, Y. Shimizu, M. Egashira, H_2 and NOx sensing properties of ZnO and In_2O_3 powders modified with mesoporous SnO_2, J. Ceram. Soc. Jpn. 112 (2004) S540–S545.

51. Y. Shimizu, K. Tsumura, T. Hyodo, M. Egashira, Effect of simultaneous modification with metal loading and mesoporous layer on H_2 sensing properties of SnO_2 thick film sensors, IEEJ Trans. SM 125 (2005) 70–74.

52. T. Hyodo, K. Sasahara, Y. Shimizu, M. Egashira, Preparation of macroporous SnO_2 films using PMMA microspheres and their sensing properties to NOx and H_2, Sens. Actuators B 106, (2005) 580–590.

53. H. Seh, T. Hyodo, H. L. Tuller, Bulk Acoustic Wave Resonator as a sensing platform for

NOx at high temperatures, Sens. Actuators B 108, (2005) 547–552.

54. Y. Takakura, T. Hyodo, Y. Shiimizu, M. Egashira, Preparation of macroporous Eu-doped oxide thick films and their application to gas sensor materials, IEEJ Trans. SM 128 (2008) 137–140.

55. S. Nonaka, T. Hyodo, Y. Shiimizu, M. Egashira, Preparation of macroporous semiconductor gas sensors and their odor sensing properties, IEEJ Trans. SM 128 (2008) 141–144.

56. M. Morio, T. Hyodo, Y. Shiimizu, M. Egashira, Effect of macrostructural control of an auxiliary layer on the CO_2 sensing properties of NASICON-based gas sensors, Sens. Actuators B 139 (2009) 563–569.

57. C. Ishibashi, T. Hyodo, Y. Shimizu, M. Egashira, H_2S sensing properties of macroporous In_2O_3-based sensors, Sensor Lett., 9 (2011) 369–373.

58. K. Hieda, T. Hyodo, Y. Shimizu, M. Egashira, Preparation of porous tin dioxide powder by ultrasonic spray pyrolysis and their application to sensor materials, Sens. Actuators B 133 (2008) 144–150.

59. M. Hashimoto, H. Inoue, T. Hyodo, Y. Shimizu, M. Egashira, Preparation and gas sensor application of ceramic particles with submicron-size spherical macropores, Sensor Lett. 6 (2008) 887–890.

60. A. Anaraki Firooz, T. Hyodo, A. R. Mahjoub, A. A. Khodadadi, Y. Shimizu, Synthesis of nano- and meso-porous MoO_3-doped SnO_2 as a selective gas-sensing material to NO_2, Sens. Actuators B 147 (2010) 5544–5560.

61. T. Hyodo, H. Inoue, H. Motomura, K. Matsuo, T. Hashishin, J. Tamaki, Y. Shimizu, M. Egashira, NO_2 sensing properties of macroporous In_2O_3-based powders fabricated by utilizing ultrasonic spray pyrolysis employing polymethylmethacrylate microspheres as a template, Sens. Actuators B 151 (2010) 265–273.

62. T. Hyodo, A. Bieberle-Hütter, J. L. Hertz, H. L. Tuller, Three dimensional arrays of hollow

gadolinia-doped ceria microspheres prepared by r.f. magnetron sputtering employing PMMA microsphere templates, J. Electroceram. 17 (2006) 695–699.

63. I.-D. Kim, A. Rothschild, T. Hyodo, H. L. Tuller, Microsphere templating as means of enhancing surface activity and gas sensitivity of $CaCu_3Ti_4O_{12}$ thin films, Nano Lett. 6 (2006) 193–198.
64. E. Fujii, T. Hyodo, K. Matsuo, Y. Shimizu, NO_2 sensing properties of porous In_2O_3-based powders prepared by utilizing ultrasonic-spray pyrolysis employing PMMA microsphere templates: Effects of the size of the PMMA microspheres on their gas-sensing properties, ECS Trans. 50(12) (2012) 273-278.
65. T. Hyodo, S. Furuno, E. Fujii, K. Matsuo, S. Motokucho, K. Kojio, Y. Shimizu, Porous In_2O_3 powders prepared by ultrasonic-spray pyrolysis as a NO_2-sensing material: Utilization of polymethylmethacrylate microspheres synthesized by ultrasonic-assisted emulsion polymerization as a template, Sens. Actuators B 187 (2013) 495–502.
66. The Merck Index, 13th Ed., Ed. by M. J. O'Neil, Merck & Co., Inc., p. 890 (2001).

Figure Captions

Fig. 1. Variation in conversion ratio from MMA to PMMA with sonication time and representative particle-size distributions of PMMA microspheres synthesized in o/w emulsion.

Fig. 2. Pore-size distributions of representative pr-In_2O_3(T_p) powders as-prepared and after heat treatment at 550ºC for 5 h, together with their specific surface area (SSA).

Fig. 3. SEM photographs of representative pr-In_2O_3(T_p) powders as-prepared and after heat treatment at 550ºC for 5 h.

Fig. 4. TEM photographs of representative pr-In_2O_3(T_p) powders as-prepared and after heat treatment at 550ºC for 5 h.

Fig. 5. Variations in crystallite size (CS) and specific surface area (SSA) of pr-In_2O_3(T_p) powders as-prepared and after heat treatment at 550ºC for 5 h (open symbols) with pyrolysis temperature (T_p), together with those of representative c-In_2O_3(T_p) powders as-prepared and after heat treatment at 550ºC for 5 h (filled symbols). HT: heat treatment.

Fig. 6. SEM and TEM photographs of as-prepared c-In_2O_3(*1100*) powder.

Fig. 7. Response transients of pr-In_2O_3(*600*), pr-In_2O_3(*1100*), and c-In_2O_3(*1100*) sensors to 10 ppm NO_2 at 200ºC in dry air. FT: thickness of the In_2O_3 films.

Fig. 8. Variations in response of pr-In_2O_3(*600*), pr-In_2O_3(*1100*), and c-In_2O_3(*1100*) sensors to 10 ppm NO_2 in dry air and their 90% response time with operating temperature. FT: thickness of the In_2O_3 films.

Fig. 9. Variations in response of pr-In_2O_3(*600*), pr-In_2O_3(*1100*), and c-In_2O_3(*1100*) sensors to 1 and 5 ppm NO_2 in dry air with operating temperature. FT: thickness of the In_2O_3 films.

Fig. 10. Variations in average particle size of PMMA microspheres and conversion ratio from

MMA to PMMA after 30 min with the amount of SLS added to deionized water (100 cm^3). Inserted figure (i): particle-size distribution of PMMA microspheres synthesized in o/w emulsion containing 0.5 g SLS.

Fig. 11. Pore-size distributions of pr-In_2O_3(*1100*)S powders as-prepared and after heat treatment at 550ºC for 5 h, together with their SSA and CS. The CS was calculated from their XRD patterns, but they were not shown in this paper.

Fig. 12. SEM and TEM photographs of as-prepared pr-In_2O_3(*1100*)S powder.

Fig. 13. Response transients of pr-In_2O_3(*1100*)S sensor (thickness of the In_2O_3 film (FT): ca. 20 μm) to 10 ppm NO_2 at 200ºC in dry air, together with those of pr-In_2O_3(*1100*) and c-In_2O_3(*1100*) sensors as references.

Fig. 14. Variations in response of pr-In_2O_3(*1100*)S sensor to 10 ppm NO_2 in dry air and the 90% response time with operating temperature, together with those of pr-In_2O_3(*1100*) and c-In_2O_3(*1100*) sensors as references. FT: thickness of the In_2O_3 films.

Fig. 15. Variations in response of pr-In_2O_3(*1100*)S, pr-In_2O_3(*1100*), and c-In_2O_3(*1100*) sensors to 1 and 5 ppm NO_2 in dry air with operating temperature. Inserted figures (i) and (ii): response transients of pr-In_2O_3(*1100*)S sensor to 1 and 5 ppm NO_2. FT: thickness of the In_2O_3 films.

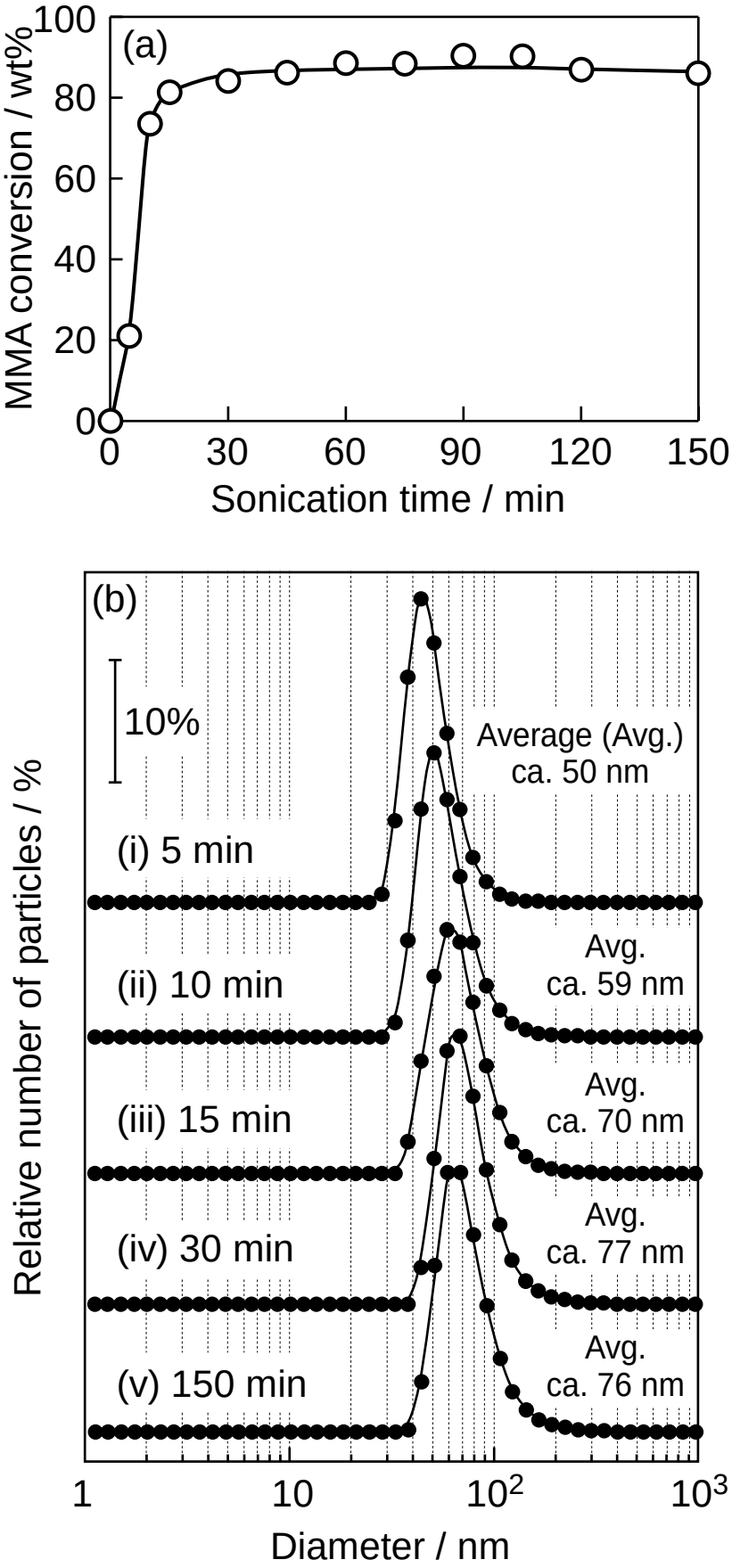

Fig. 1. Hyodo et al.

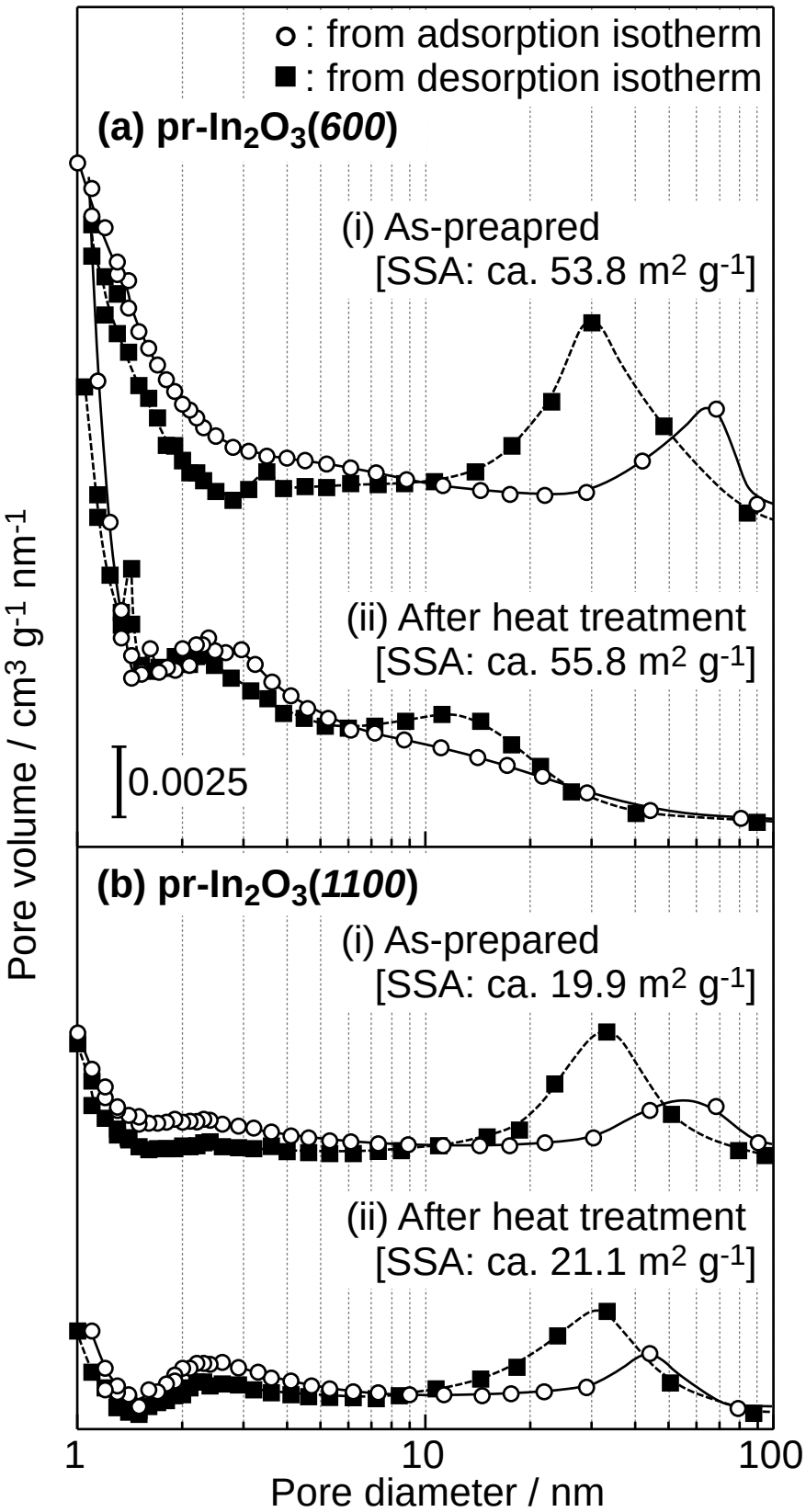

Fig. 2. Hyodo et al.

(a) pr-In_2O_3(*600*)

(i) As-prepared

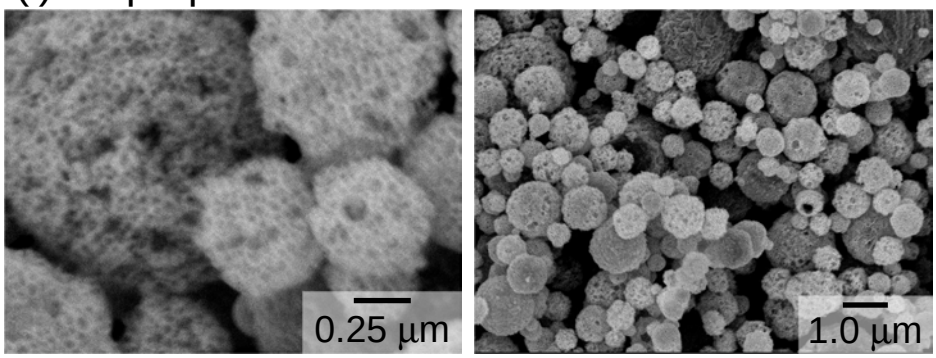

(ii) After heat treatment

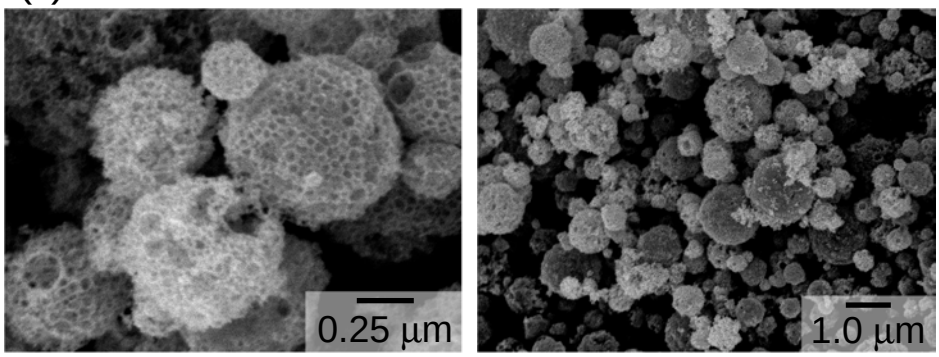

(b) pr-In_2O_3(*1100*)

(i) As-prepared

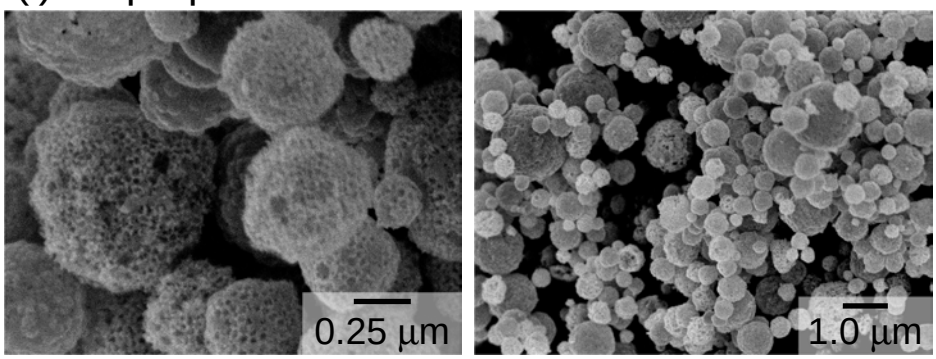

(ii) After heat treatment

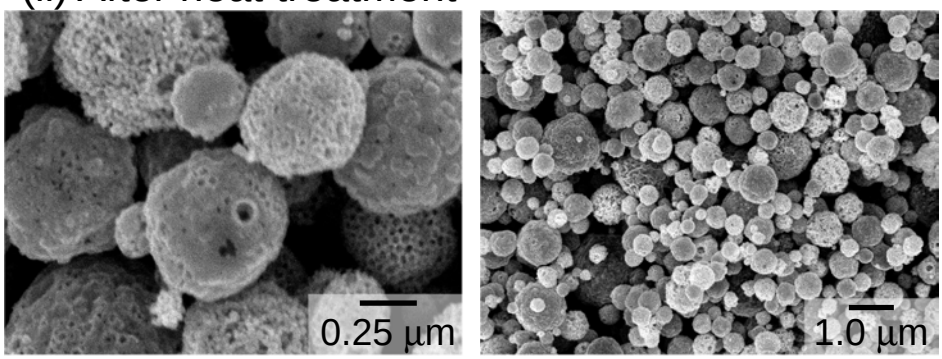

Fig. 3. Hyodo et al.

(a) pr-In_2O_3(*600*)

(i) As-prepared

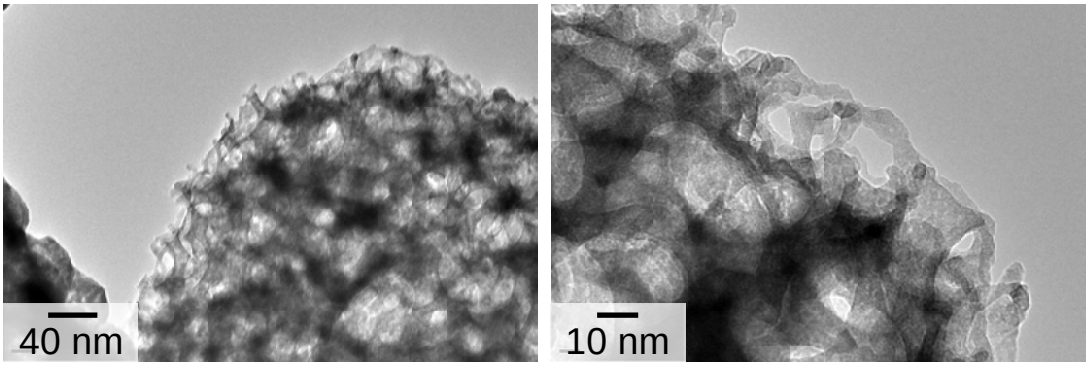

(ii) After heat treatment

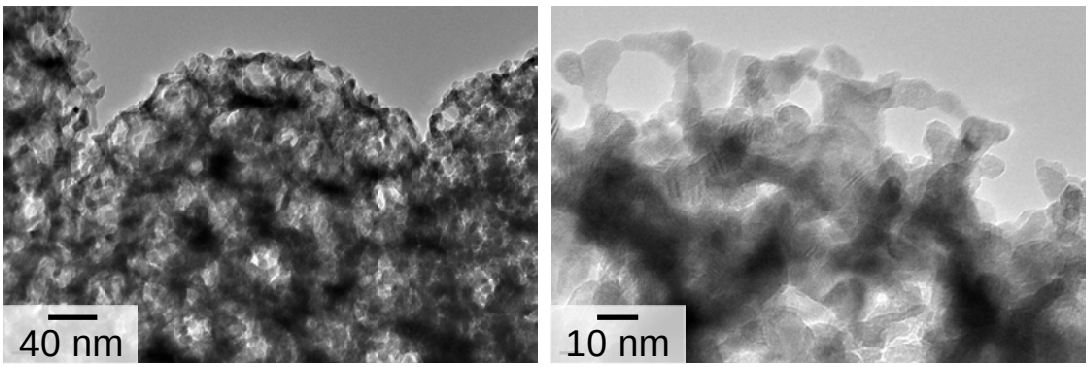

(b) pr-In_2O_3(*1100*)

(i) As-prepared

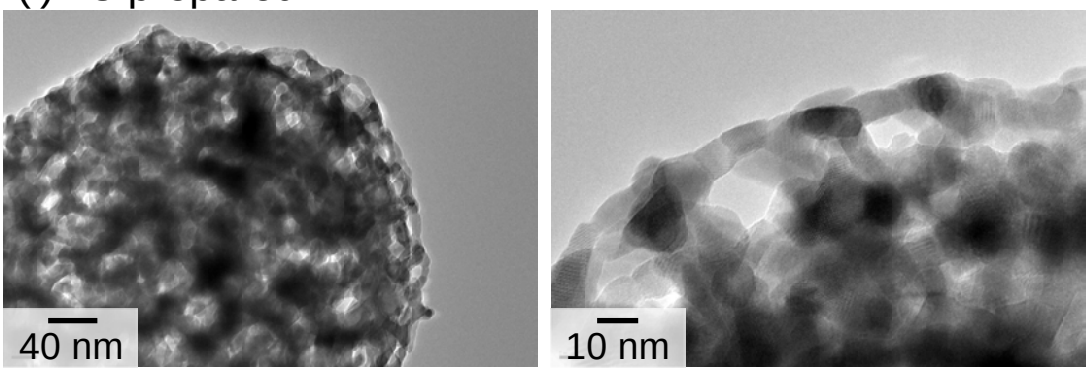

(ii) After heat treatment

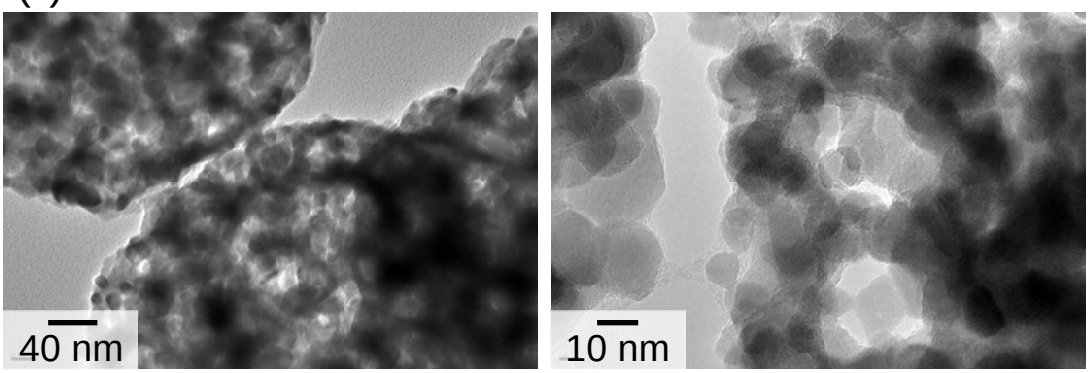

Fig. 4. Hyodo et al.

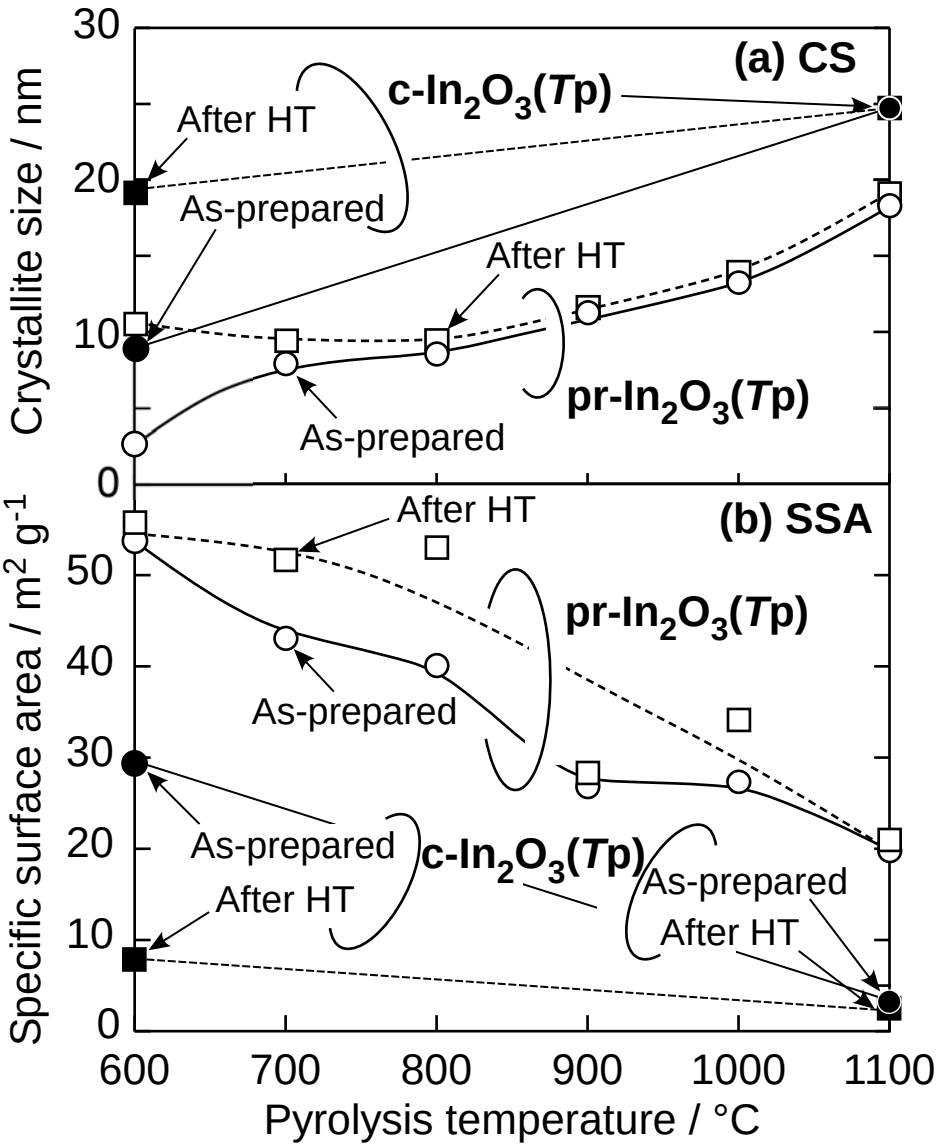

Fig. 5. Hyodo et al.

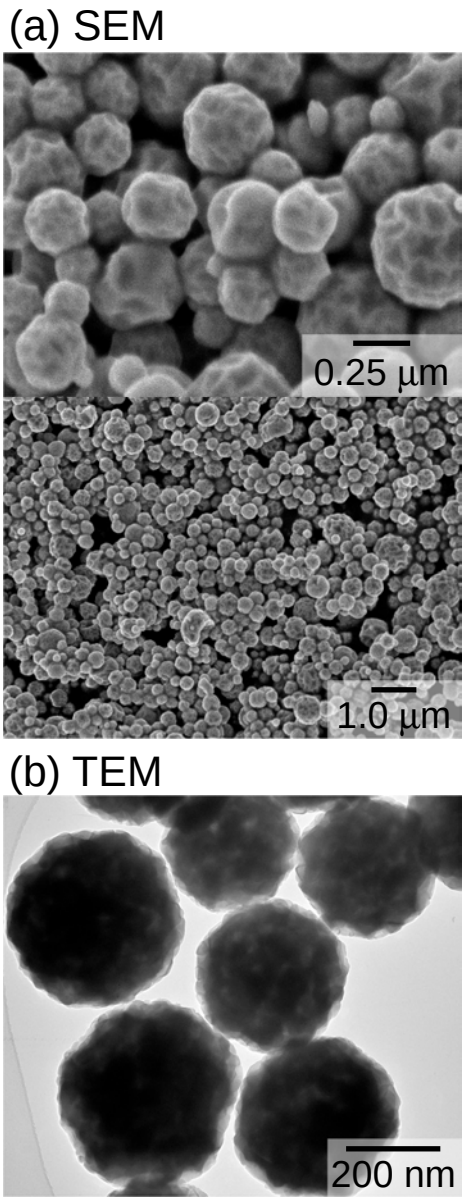

Fig. 6. Hyodo et al.

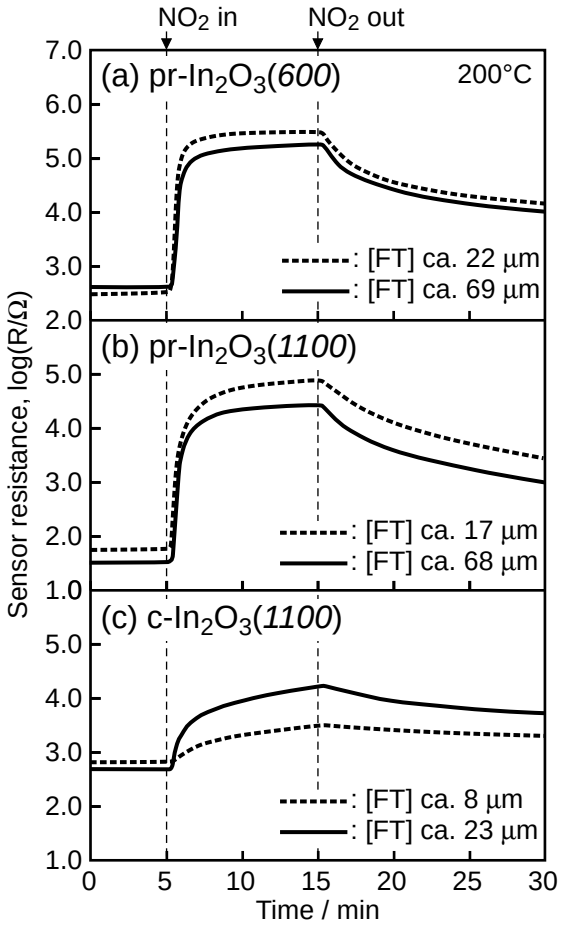

Fig. 7. Hyodo et al.

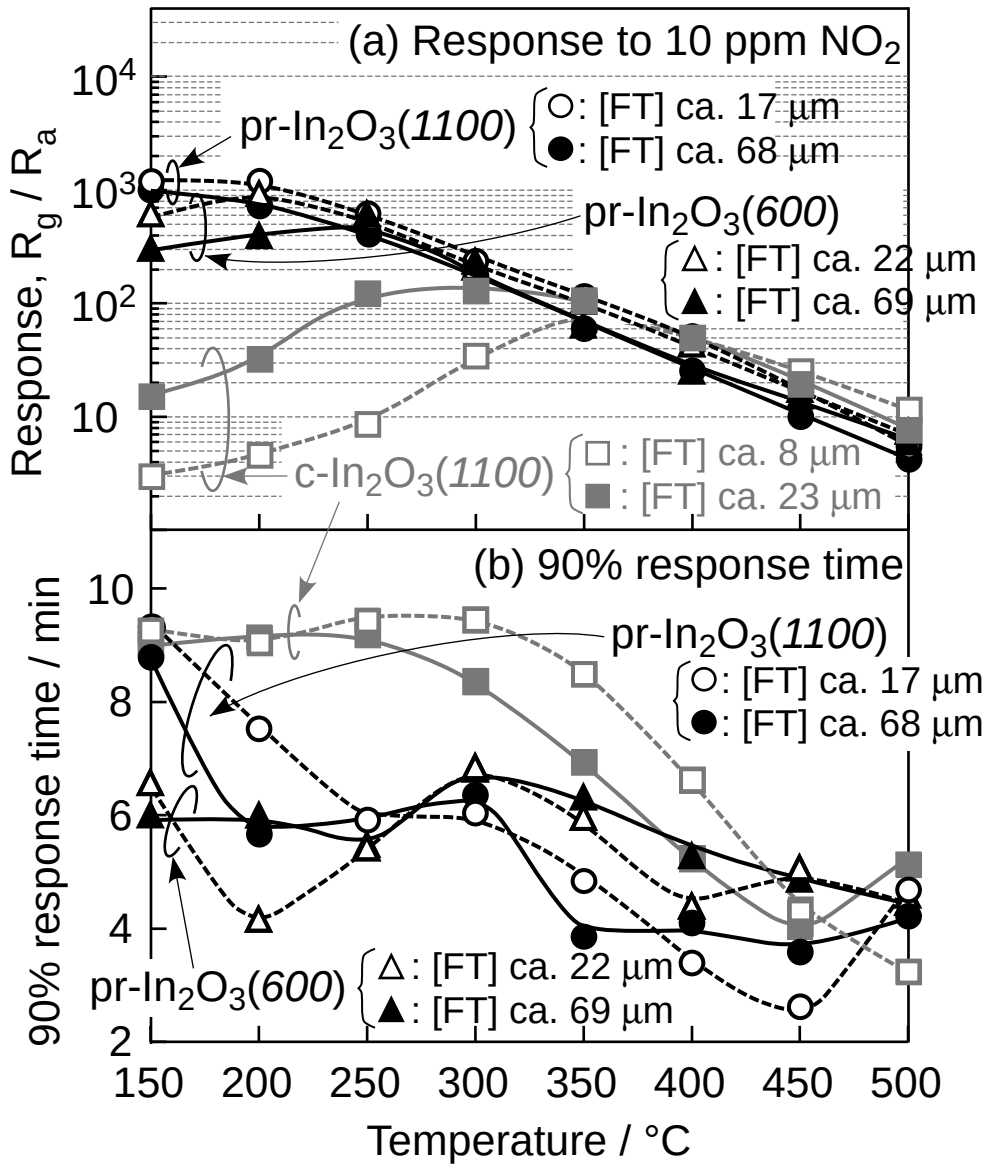

Fig. 8. Hyodo et al.

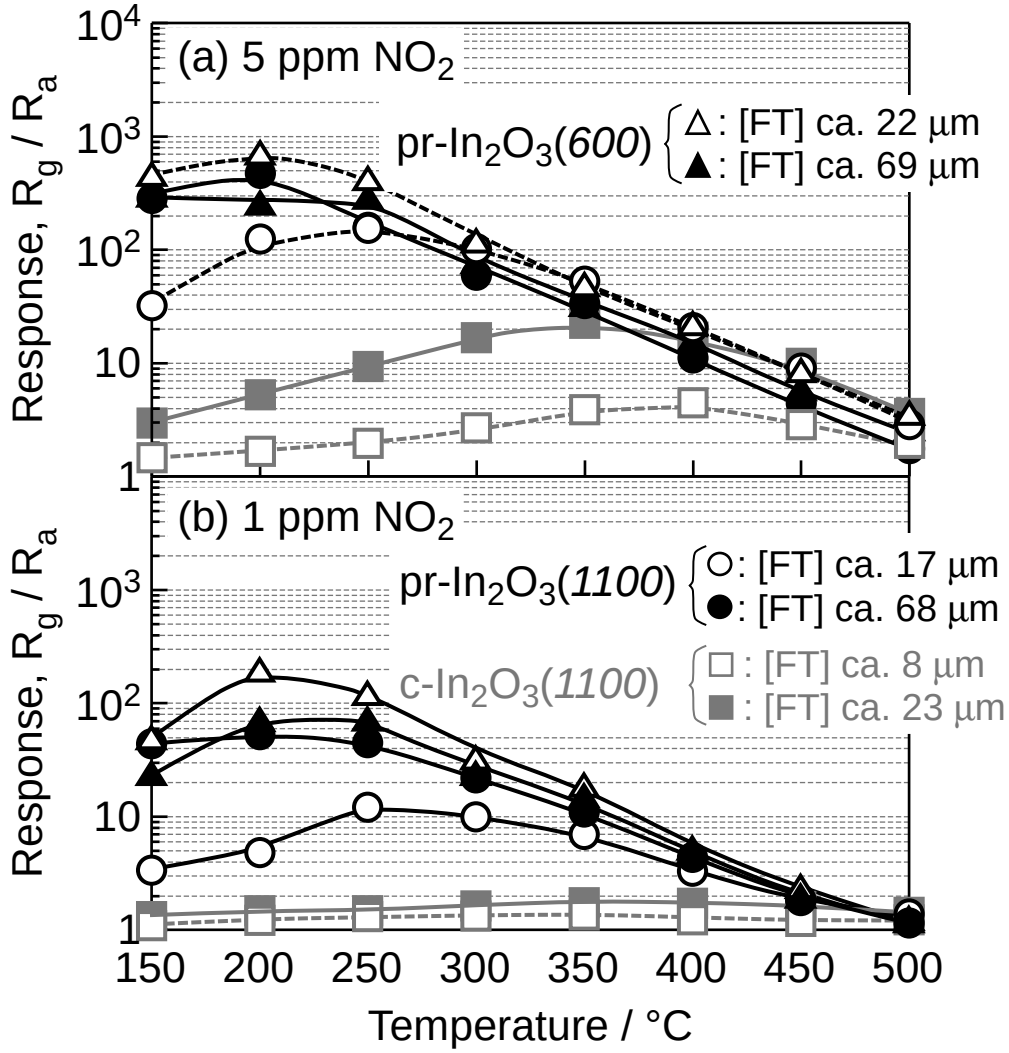

Fig. 9. Hyodo et al.

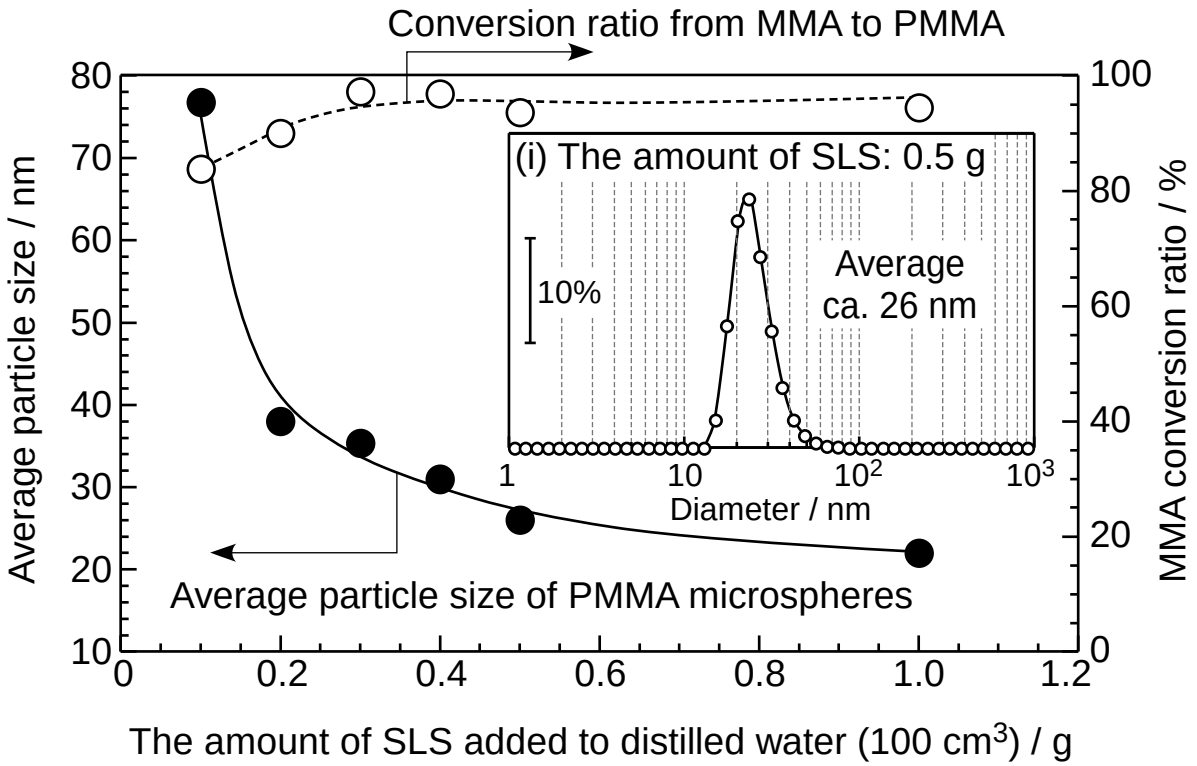

Fig. 10. Hyodo et al.

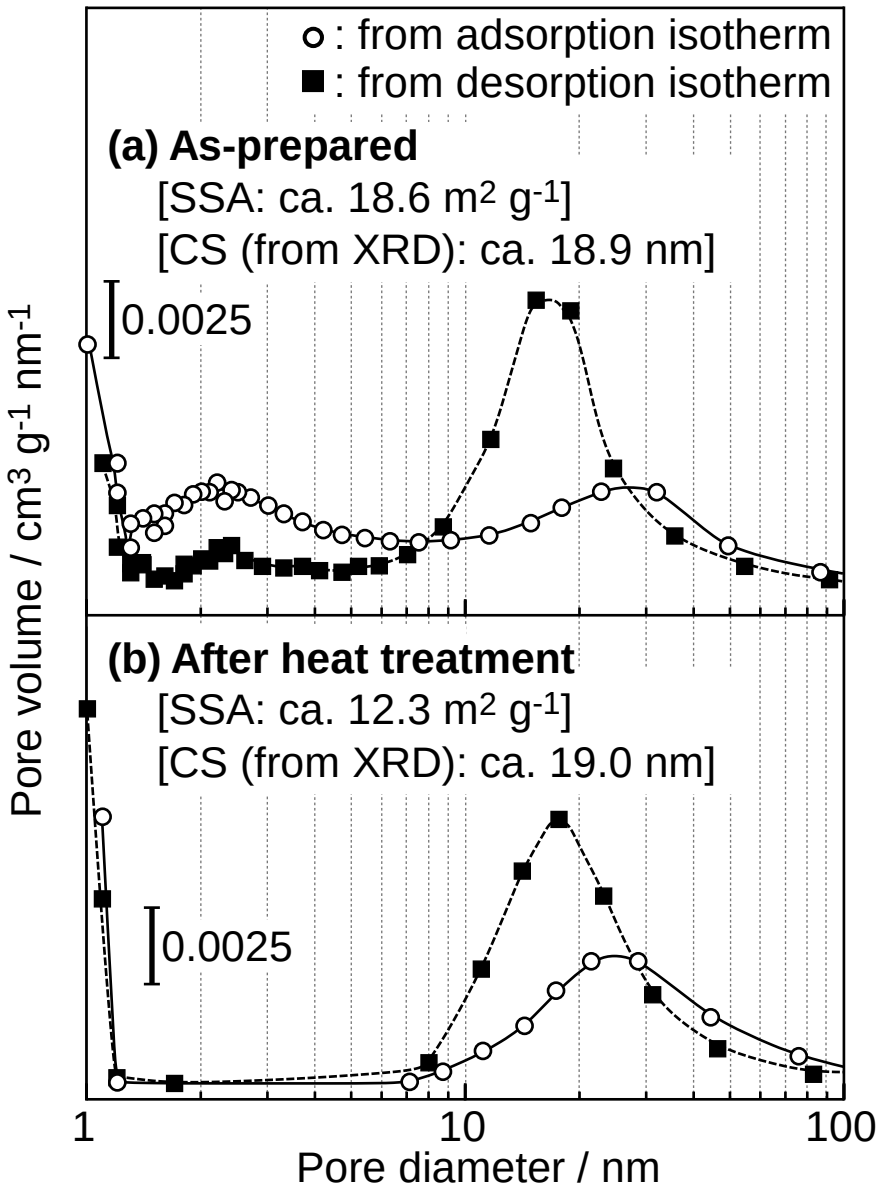

Fig. 11. Hyodo et al.

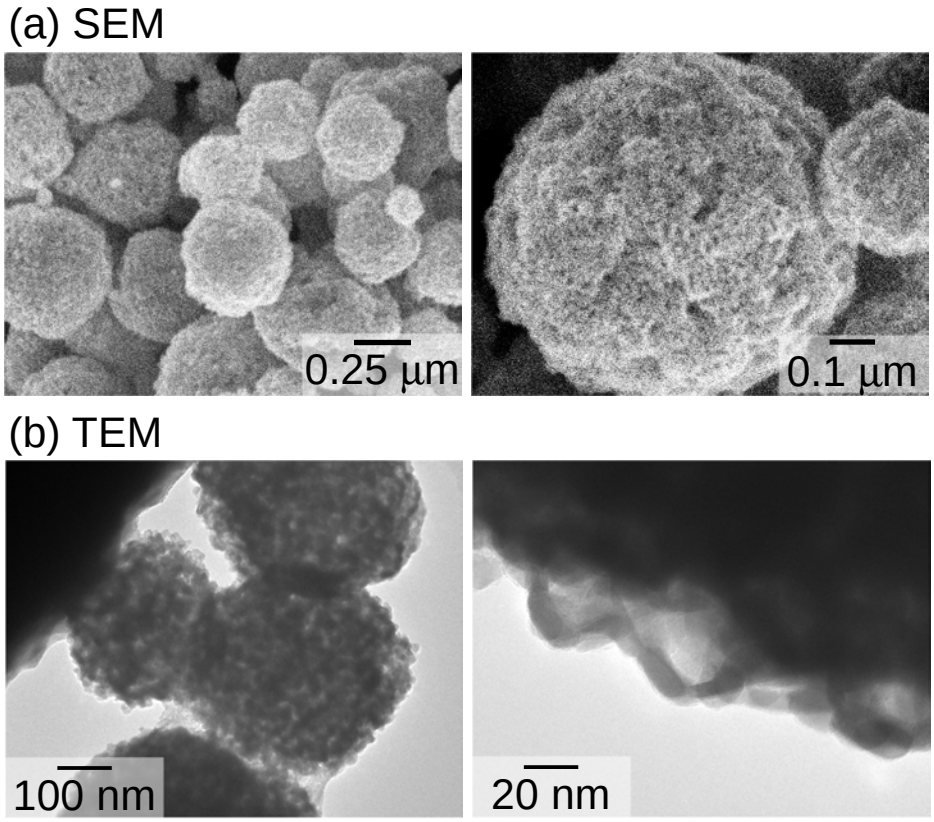

Fig. 12. Hyodo et al.

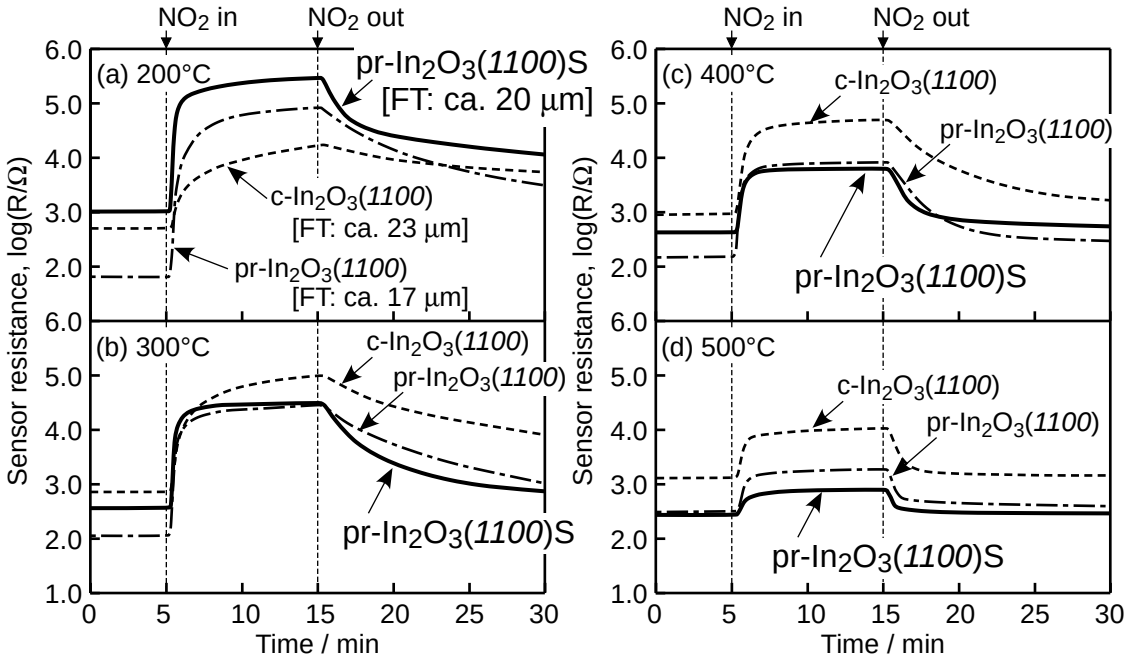

Fig. 13. Hyodo et al.

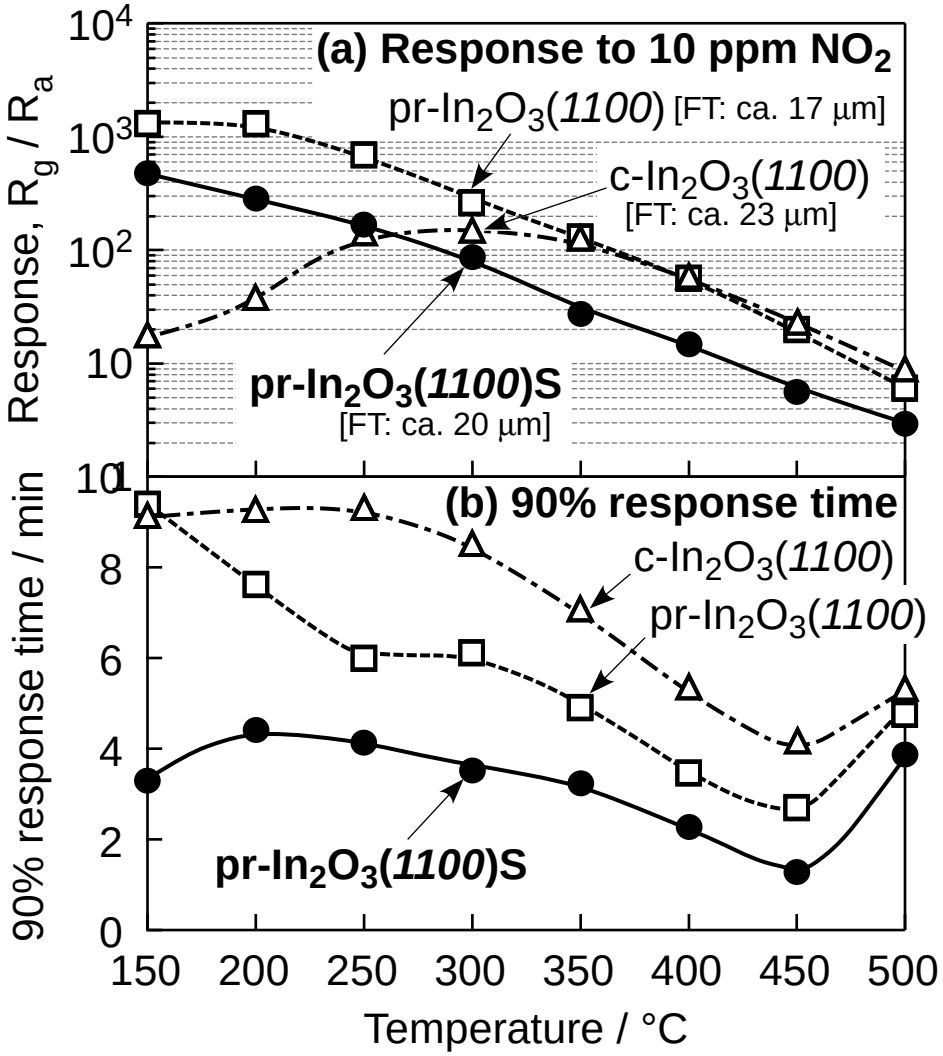

Fig. 14. Hyodo et al.

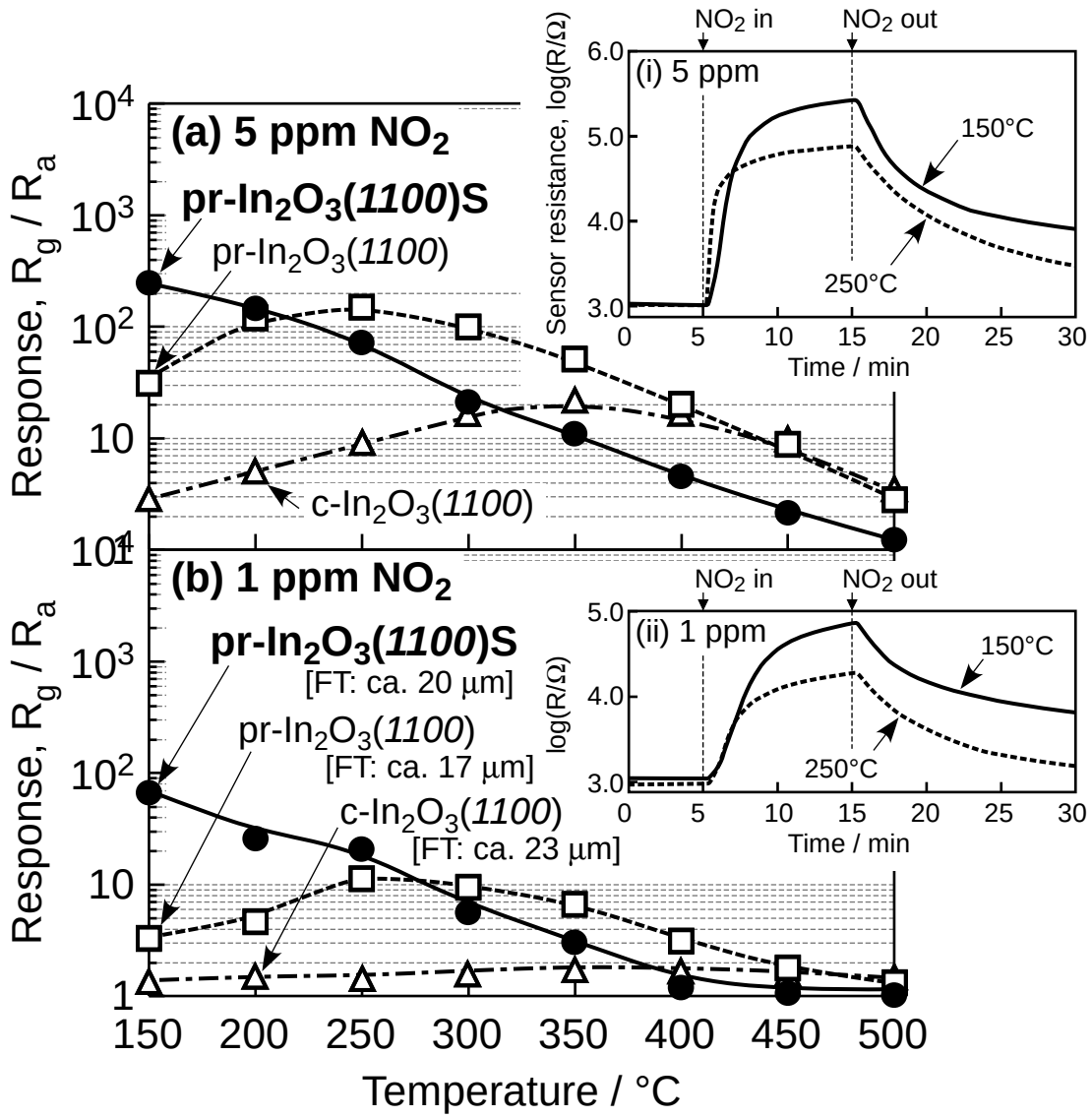

Fig. 15. Hyodo et al.